Left-right symmetry at an FCC-hh

Miha Nemevšek[1,2,*] and Fabrizio Nesti[3,4,†]

[1]*Jožef Stefan Institute, Jamova 39, 1000 Ljubljana, Slovenia*
[2]*Faculty of Mathematics and Physics, University of Ljubljana, Jadranska 19, 1000 Ljubljana, Slovenia*
[3]*Dipartimento di Scienze Fisiche e Chimiche, Università dell'Aquila, via Vetoio, I-67100 L'Aquila, Italy*
[4]*INFN, Laboratori Nazionali del Gran Sasso, I-67100 Assergi (AQ), Italy*

We study the production of right-handed bosons W_R and heavy neutrinos N at a future 100 TeV high-energy hadron collider in the context of left-right symmetry, including the effects of W_L-W_R gauge boson mixing. We estimate the collider reach for up to 3/ab integrated luminosity using a multibinned sensitivity measure. In the Keung-Senjanović and missing-energy channels, the 3σ sensitivity extends up to $M_{W_R} = 35$ and 37 TeV, respectively. We further clarify the interplay between the missing-energy channel and the (expected) limits from neutrinoless double beta decay searches and big bang nucleosynthesis (and dark matter).

I. INTRODUCTION

With the enduring experimental successes of the Standard Model (SM), it is striking that we still lack a definitive theory of neutrino masses. A hint for going beyond the SM might be found in its structure, where the fermion quantum numbers seem to point to an underlying parity-symmetric theory. This is in sharp contrast with the maximal breaking of parity observed in the weak sector. This clash was resolved in the left-right (LR) symmetric theories [1–6] and turned out to be deeply connected with the issue of neutrino mass origin.

In the minimal LR symmetric model (LRSM), parity is broken spontaneously [3–6], together with the new right-handed (RH) weak gauge group $SU(2)_R$. The fermion sector then keeps the parity symmetry, while the gauge sector does not. Spontaneous symmetry breaking is triggered by a $SU(2)_R$ triplet scalar Δ_R that simultaneously generates the masses of additional gauge bosons W_R and Z_{LR}, as well as the masses for RH neutrinos N. Their masses mainly come from a Majorana-type Yukawa term that generates the N mass and breaks the total lepton number after Δ_R gets a vacuum expectation value (VEV). The residual SM gauge group is then finally broken via a LR bidoublet scalar field, which contains the SM Higgs

doublet h and an extra heavier doublet H. The bidoublet has two VEVs that may give rise to a mixing of the SM W and W_R. After the completion of electroweak breaking, light neutrinos also get their Majorana masses with contributions from the celebrated seesaw mechanism [5–9].

In general, to uncover the true microscopic picture of particle mass origin, we need to perform direct searches at colliders and measure the masses and couplings of elementary particles, just like we did with the Higgs boson. Neutrinos are no exception, and ultimately we would need to make a direct discovery at high-energy colliders to solidify our understanding of their mass origin. Only such machines would allow us to perform direct searches for resonances, such as the W_R, and give us immediate access to heavy Majorana neutrinos N. In the golden Keung-Senjanović (KS) process [10], the W_R is Drell-Yan produced and decays into a right-handed (RH) charged lepton ℓ_R and N, see [11] for a review of LNV signals at colliders. In turn, N decays dominantly through a possibly off-shell W_R into another lepton and two jets with the exact signal depending on its mass m_N [12,13]; see Fig. 1. Owing to the Majorana nature of N, the two leptons have the same electromagnetic charge half of the time, revealing the breaking of lepton number (see Ref. [14] for departures
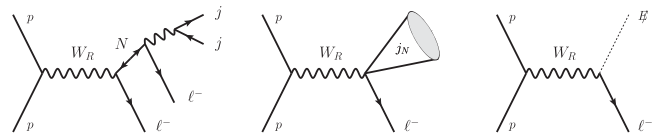
*miha.nemevsek@ijs.si
†fabrizio.nesti@aquila.infn.it

FIG. 1. Final states of the W_R production, with a prompt charged lepton plus N decay products, including a lepton and jets (KS, left), a prompt merged j_N (center), and missing energy (right).

from pure Majorana states). Lighter N becomes boosted, and its decay products collimate into a single neutrino jet [15]. Finally, if N is below ~ 100 GeV, it becomes long-lived and manifests itself as a lepton plus missing-energy $\ell \not{E}$ signature [13]. The current LHC searches cover the range of well-separated objects in $\ell \ell j j$ [16–18], collimated "neutrino" jets [17–19], and leptons with missing energy [20].

The above W_R searches quickly lose sensitivity when N is progressively off shell, $m_N > M_{W_R}$. In such case, one can resort to neutrinoless final states, such as dijets and pairs of SM gauge bosons that appear in the presence of W_L-W_R mixing. The dijet resonance searches were performed in Refs. [21,22], the heavy quark final state $W_R \to tb$ was looked for in Refs. [23,24], and the $W_R \to WZ$ channel was sought in Ref. [25]. All these limits converge into a current lower bound on M_{W_R} in the range of 4–5.7 TeV. The expected reach of the LHC can further extend to 6–7 TeV with large statistics [26], so the parameter space accessible by LHC is almost covered. The aim of this work is to provide a definitive outlook for the 100 TeV hadronic colliders, and to connect it to low-energy processes and to the physics of the early Universe.

Apart from the existing collider searches, the precision frontier at low energies also delivers a set of stringent constraints. It was known since the early days [27] that loop-induced flavor-changing processes in the K-meson sector push the W_R scale into the few TeV regime. Moreover, the LRSM contains an additional doublet H with flavor off-diagonal couplings that mediate flavor-changing processes even at tree level, which push the LR scale even higher [28]. A number of subsequent works have addressed these issues [29–33]. The most recent updates [34] uncovered the dominant role of B-meson oscillations and set the limits in the ballpark of $M_{W_R} \gtrsim 8$ TeV and $M_H \gtrsim 20$ TeV. Even if such M_{W_R} values may still be marginally or indirectly probed by the LHC, the heavier H implies that the model has to live at the brink of nonperturbativity [35,36]. A heavier M_{W_R} would clearly relax this tension.

In parallel, constraints from CP violation come from the interplay between the neutron electric dipole moment and meson processes [37,38]. These would require M_{W_R} to be pushed beyond 10–20 TeV, at least if LR parity $\mathcal{P}$ is adopted; see Ref. [39] for the discussion of parity as gauge symmetry and the nature of its imposition. And even if an axion is invoked, CP violation still implies lower bounds in the ballpark of 10–20 TeV [40]. In case of $\mathcal{C}$ as LR parity, the additional CP phases are sufficient in order to accommodate all the CP-violating channels, and such bounds go away.

In summary, the LRSM scale is being driven to ever larger scales of $\mathcal{O}(10)$ TeV, nearly out of reach of the LHC, but easily probed by a future 100 TeV hadron collider (FCC). A number of studies have started addressing this scenario [41–44]; see also Refs. [45] and [46]. However, a complete assessment of the FCC potential for the LRSM,

including the simulation of backgrounds and transitions between different regimes of m_N, is still missing. In this work, we close this gap and clarify the FCC reach by taking into account the standard KS and missing-energy channels.

In addition to the usual W_R channels, we address the role of the LR gauge boson mixing ξ_{LR}, which leads to an interplay between the production and decay via the SM W. These channels are complemented by those mediated by Dirac Yukawa couplings that are responsible for the mixing between the light and heavy Majorana neutrinos. With an input from neutrino oscillations and masses/mixings of N, one can disentangle the seesaw and compute the Dirac mass matrix for both choices of LR parity: $\mathcal{C}$ [47] and $\mathcal{P}$ [48–50]. We show that their effect is relevant in the very light RH neutrino mass range. Here, displaced signatures play a major role [26] and shall be the subject of dedicated studies once the detector geometries and efficiencies are known for the FCC-hh.

Apart from the involved analyses using displaced vertices, the missing-energy signal can be understood and estimated quite reliably. It is precisely in this region of parameter space that interesting connections with other processes arise as well. It turns out that the neutrinoless double beta ($0\nu\beta\beta$) decay rate from N exchange [51] and from additional mixed diagrams [52] is able to compete with FCC-hh, given the (optimistic) sensitivity of forthcoming experiments. Finally, we should point out the connection to dark matter in the LRSM [53,54] that may reside in the 20 TeV range [54] but is also subject to additional constraints from large-scale structures [55].

In Sec. II, we review in detail the production of W_R and the decay chains of the RH neutrino N. In Sec. III, we discuss the numerical simulations of relevant backgrounds. In Sec. IV, we analyze the signal features for the relevant processes, and in Sec. V, we discuss the assessment of the expected sensitivity and present the results. Section VI contains the final discussion, and in the Appendix, we give more details and analytic derivations.

II. PRODUCTION AT THE FCC AND DECAY RATES

In this section, we review the production of W_R at a pp collider, its decay through N, including the various N decay channels, and the role of the left-right gauge boson mixing

$$|\xi_{LR}| \simeq \sin 2\beta \left(\frac{M_W}{M_{W_R}} \right)^2. \tag{1}$$

Here, $t_\beta \equiv \tan\beta = v_2/v_1$ is the ratio of the two bidoublet VEVs; see Ref. [32] for details.

A. Production of W_R …

The production of an on-shell W_R proceeds through the Drell-Yan process involving the two initial partons:

$$\frac{\mathrm{d}^2\sigma_{pp\to W_R^+}}{\mathrm{d}x_1\mathrm{d}x_2} = \frac{\pi^2\alpha_2}{N_c}\delta(\hat{s} - M_{W_R}^2)$$
$$\times \sum_{u,d}|V_{ud}|^2(f_u(x_1)f_{\bar{d}}(x_2) + 1 \leftrightarrow 2). \quad (2)$$

Here, $x_{1,2}$ are the parton momentum fractions, $\hat{s} = x_1x_2s$, and $\sqrt{s} = 100$ TeV is the center-of-mass energy; see the Appendix for a complete derivation.

The above formula also holds when the left-right gauge boson mixing ξ_{LR} is turned on (via t_β), because the contributions from the right and the left mixing currents, proportional to $\sin^2 \xi_{LR}$ and $\cos^2 \xi_{LR}$, sum up to 1, while the interference terms are suppressed either by small quark masses or by PDFs of the proton.

In the Appendix, we collect the rates of the various W_R decay channels—namely, the dijet and ℓN, as well as WZ/Wh mediated by gauge boson mixing. We find that the parent W_R is never produced with a high boost. Indeed, we find that the maximal boost factor γ is given by

$$\gamma_{W_R}^{\max} \simeq \frac{\sqrt{s}}{2M_{W_R}}. \quad (3)$$

Moreover, the W_R decay products are typically much lighter than M_{W_R}, such that they feature back-to-back geometry distinctive of two-body decays. The only relevant exception is the case of ℓN, with N being nearly as heavy as W_R, to be discussed shortly below. For completeness, we report the k-factors for the production, including NLO effects, in Sec. IV.

B. … and ℓN

The triple differential cross section for the $pp \to \ell^+N$ production via W_R^+ is given by

$$\frac{\mathrm{d}^3\sigma_{pp\to\ell^+N}}{\mathrm{d}x_1\mathrm{d}x_2\mathrm{d}\hat{t}} = \frac{\pi\alpha_2^2}{12\hat{s}^2}\frac{\hat{t}(\hat{t} - m_N^2)}{(\hat{s} - M_{W_R}^2)^2 + (\Gamma M_{W_R})^2}$$
$$\times \sum_{ud}|V_{ud}V_{\ell N}|^2(f_u(x_1)f_{\bar{d}}(x_2) + 1 \leftrightarrow 2),$$
$$(4)$$

where Γ is the total decay width of W_R, and $\hat{s}$ and $\hat{t}$ are the partonic Mandelstam variables. Integrating over $\hat{t}$ and the PDFs, we get the total cross section for $pp \to \ell N$:

$$\sigma_{pp\to\ell^+N} = \frac{\pi\alpha_2^2}{24N_c}\int_{\frac{m_N^2}{s}}^1 \mathrm{d}x_1 \int_{\frac{m_N^2}{x_1s}}^1 \mathrm{d}x_2 \frac{\hat{s}}{(\hat{s} - M_{W_R}^2)^2 + (\Gamma M_{W_R})^2}$$
$$\times \left(1 - \frac{m_N^2}{\hat{s}}\right)^2\left(2 + \frac{m_N^2}{\hat{s}}\right)$$
$$\times \sum_{ud}|V_{ud}V_{\ell N}|^2(f_u(x_1)f_{\bar{d}}(x_2) + 1 \leftrightarrow 2). \quad (5)$$

We compare the cross sections for $pp \to W_R$ from Eq. (A15) with $pp \to \ell N$ from Eq. (5) at $\sqrt{s} = 100$ TeV
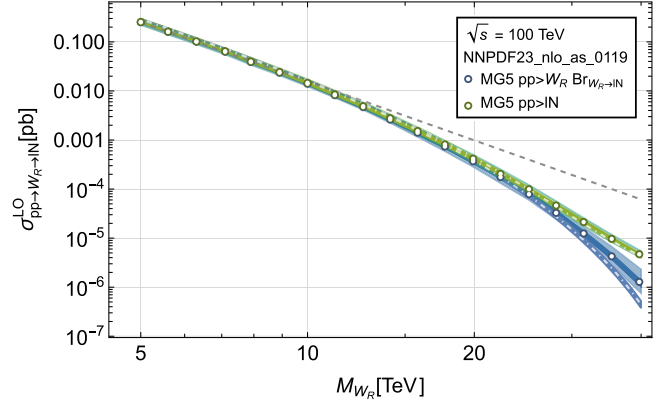

FIG. 2. The total cross section $pp \to W_R \to \ell N$, for fixed $m_N = 200$ GeV and $t_\beta = 0$. Blue dots (solid line) represent the narrow-width approximation as calculated by MadGraph (analytically). The light (dark) blue band corresponds to scale (PDF) variation. The green dots (solid line) represent the exact $pp \to \ell N$ result via MadGraph (analytics). Green bands also show the scale and PDF variations, which is smaller for $pp \to W_R \to \ell N$. The gray dashed line shows the $M_{W_R}^{-4}$ slope, normalized to 5 TeV.

and plot them in Fig. 2. These analytical calculations are shown with white dot-dashed lines and accompanied by bands that show the uncertainties due to scale variation by a factor of 2—i.e., $\mu \in [0.5, 2]\sqrt{\hat{s}}$. These are compared to the numerical results from MadGraph, shown with empty dots. They are surrounded by darker bands showing the uncertainties for scale variation and lighter bands for PDF member variation. As a rule of thumb, the cross sections fall as $M_{W_R}^{-4}$, and this naive expectation is shown by the gray dashed line. It is a very good proxy for W_R masses up to about a few tens of TeV, above which the cross sections go below this simple scaling. The narrow-width approximation in blue does pretty well compared to the exact case of $2 \to 2$ scattering (shown in green) but starts to fail at about 20 TeV, missing the relevant fraction of W_R produced off shell. It also overestimates the uncertainty in the cross section due to scale variation and PDF, as the uncertainty in the exact total cross section stays below 10%.

To better understand the dynamics in the 100 TeV regime, we move from the total integrated cross section to kinematical distributions. Let us focus first on the $p_T(\ell) = p_T(N)$ distribution of the leading lepton, shown in the upper frame of Fig. 3 for various M_{W_R} and m_N. One can distinguish the two regimes of off- and on-shell W_R on the left and right portions of each line. Clearly, the maximal p_T of the lepton (and RH neutrino) is limited by the W_R mass and by the center-of-mass energy via the PDFs. For W_R produced at rest, which is the relevant regime for large M_{W_R}, one has

$$p_T^{\max}(\ell_1) \simeq \frac{M_{W_R}}{2}\left(1 - \frac{m_N^2}{M_{W_R}^2}\right). \quad (6)$$
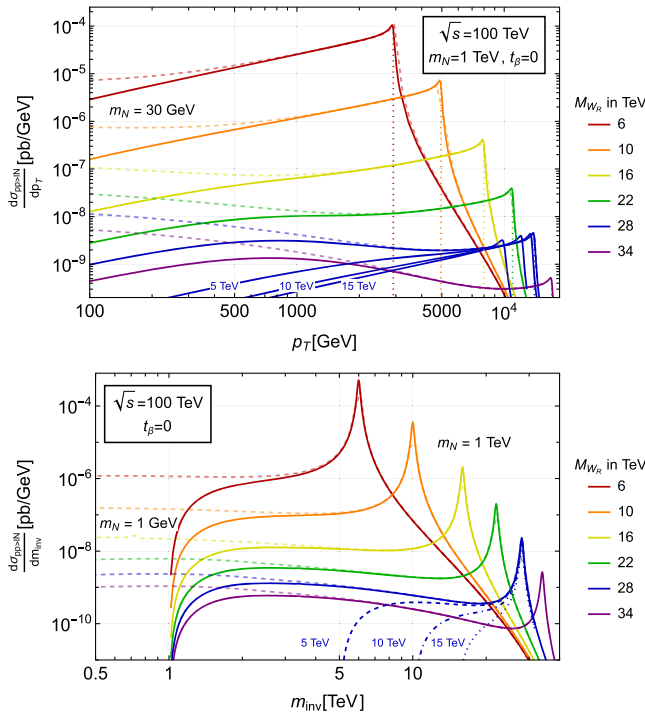
FIG. 3. Leading lepton $p_T(\ell_1)$ distribution (top) and invariant mass of ℓN (bottom) in the $pp \to \ell N$ production at $\sqrt{s} = 100$ TeV. Solid lines are $m_N = 1$ TeV, while the dotted, dot-dashed, and dashed lines are 5, 10, and 15 TeV, respectively. On the p_T plot, we plot the vertical dotted lines of $p_T^{\max}(\ell_1)$ from Eq. (6), and the color dashed lines are for $m_N = 30$ GeV. In the invariant mass plot below, the dashed lines correspond to $m_N = 1$ GeV.

This is derived from Eq. (A42) with an on-shell W_R—i.e., by setting $\sqrt{s} = M_{W_R}$ and neglecting the masses of charged leptons and protons. As seen from the upper frame of Fig. 3, where $p_T^{\max}(\ell_1)$ from Eq. (6) is plotted with vertical dotted lines, the maximal p_T increases with M_{W_R} when N is light. It starts to decrease when m_N goes closer to the threshold of M_{W_R}, because N is produced progressively at rest.

The spectrum at low p_T is dominated by the off-shell W_R production, which is increasingly important for heavier W_R. The available effective W_R invariant mass is limited by the center-of-mass energy via the PDFs to a few TeV (dashed lines). The cross section also gets suppressed as N gets heavier, and together with the lowering of $p_T^{\max}(\ell_1)$ as described above, one ends up with a single peak in the intermediate region (blue solid lines in Fig. 3).

When t_β is turned on, additional W_R decays open up, specifically into WZ and Wh, which slightly reduces the branching ratio to $\ell_R N$. On the other hand, the production of $\ell_R N$ via W exchange and gauge boson mixing becomes possible. This leads to an increase of events at the lower end of the m_N spectrum, similar to the off-shell W_R case and is clearly favored for $m_N < M_W$.

In the lower frame of Fig. 3, we display similar useful distributions of the total invariant mass $m_{\rm inv}(\ell N)$ of the ℓ-N system. The most obvious feature is the characteristic peak at M_{W_R}. Its behavior at lower invariant masses is also interesting. For larger W_R masses, there is a significant off-shell plateau at lower invariant masses—see, e.g., the $M_{W_R} = 34$ TeV solid and dashed lines. This is quite sensitive to the mass of N and is essentially cut off below m_N, as shown in the various blue lines for $M_{W_R} = 28$ TeV.

Before moving to the decay of N, we remark that in the present work, we assume for definiteness that other possible processes in the LRSM do not interfere with the W_R and N production. In particular, given the high scales involved, one may consider the possibility that the charged components of the bidoublet or triplets have a mass in the probed regime. Their effect, together with the W_R channel, considerably complicates the signatures, due to the number of diverse couplings and mass scales involved. On the other hand, such studies will become necessary in case a signal beyond the Standard Model is observed. In the literature, some of these cases were considered as benchmarks, namely the $H^\pm$ or $\Delta_R^{\pm\pm}$ production—see, e.g. Refs. [43,44,56–59]. Also, a dedicated study of Δ^0 would be particularly interesting, since $\Delta^0 \to NN$ channel can reveal the spontaneous mass origin of m_N and probes lepton number violation in the Higgs sector [60,61]. Moreover, these channels may benefit from the large gluon-fusion production cross section at $\sqrt{s} = 100$ TeV.

C. N decay

The RH neutrino N is typically short lived if the LR scales are in the TeV region. It decays into a secondary charged lepton ℓ_2 and dominantly via an off-shell W_R into two partons—i.e., $N \to \ell q\bar{q}$. Depending on m_N and the resulting boost, the signature varies—from the lepton and two distinct jets, to the lepton and a single jet, to a single jet including the lepton. For very low m_N, the lifetime can be long enough that the decay happens at a macroscopical distance within or even outside the detector, ending up as missing energy; see Fig. 1.

The dominant N decay width is given by

$$\Gamma_{N \to \ell^\pm q_i \bar{q}_j} = 2 \frac{\alpha_2^2 m_N^5}{128\pi M_{W_R}^4} |V_{ij}^{\rm CKM}|^2$$
$$\times (1 - 8x + 8x^2 - x^4 - 12x^2 \log x), \quad (7)$$

where $x = m_q^2/m_N^2$ is the heavier quark mass of the two $m_q = \max(m_i, m_j)$. In case m_N goes below M_W, the same final states (with opposite quark chirality) can also be obtained via the standard W exchange and LR gauge boson mixing, by multiplying Eq. (7) by $\sin(2\beta)^2$.

In turn, two-body decay channels $N \to \ell W$ open up as soon as $m_N > M_W$, both in the presence of LR mixing ξ_{LR}
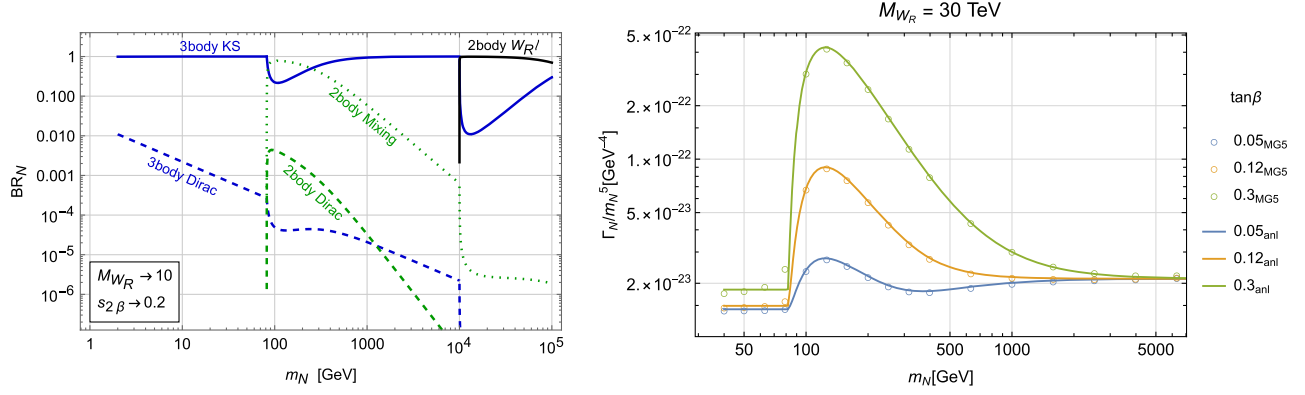
FIG. 4. Decay modes of N. On the left, we show the branching ratios for N decaying to different decay channels. On the right, we plot the t_β dependence of the total N width in the relevant mass range. The empty circles refer to the numerical output from MadGraph and the solid lines correspond to the analytic rates from Eqs. (7) and (8).

and from the mixing angle θ that connects the left- and right-handed neutrinos via the Dirac mass term. These two can be grouped together into

$$\Gamma_{N \to \ell^\pm W^\mp} = \frac{\alpha_2}{8} m_N (\theta^2 + \xi_{LR}^2) \left(\frac{1}{x} - x \right), \qquad (8)$$

with $x = M_W^2 / m_N^2 < 1$, where we have dropped a small interference term.

Finally, above $m_N > M_{W_R}$, the $N \to \ell W_R$ channel becomes dominant. It is obtained by the above formula [Eq. (8)] by replacing $M_W \to M_{W_R}$ and $\theta^2 + \xi_{LR}^2 \to 1$.

The relative weight of the various N decay channels described above can be understood collectively in a "spaghetti" plot, presented in Fig. 4 (left), which we exemplify for the case of $M_{W_R} = 10$ TeV and a moderate value of $s_{2\beta} = 0.2$. The presence of the gauge boson mixing allows for the two-body N decay, starting from $m_N \geq M_W$, to a few hundreds or thousands of GeV, depending on t_β.

On the right frame of Fig. 4, the effect of t_β on the total N width can be appreciated for $t_\beta = 0.05, 0.12, 0.3$. It is evident that t_β only impacts the light N below a few hundred GeV. It is worth recalling here that the allowed values of t_β are different in case the LR symmetry is chosen to be either $\mathcal{P}$ or $\mathcal{C}$. In the former case of $\mathcal{P}$, it is limited by flavor bounds near the value $t_\beta \simeq 0.12$ at low M_{W_R} [38], while in the latter case, it is free up to the perturbativity limit of $t_\beta \lesssim 0.5$. In this work, we adopt $t_\beta = 0.3$ as our highest benchmark value.

The dominance of the various decay channels while varying the model parameters in the M_{W_R}-m_N plane can be appreciated also in Fig. 5. Here it is notable that the two-body-mixing-mediated decays become dominant in a region just above M_W, as will be evident in the final results.

The processes mediated by Dirac neutrino masses turn out to be subleading, or relevant only in the hardly accessible high M_{W_R} and displaced N regime. The reason

lies in the small magnitude of the Dirac masses, after recalling that they are in general not free, but are predicted by the LRSM model in connection with the Majorana neutrino mass matrix [47].

In fact, the regime of very light N is particularly interesting and promising. For $m_N \lesssim 100$ GeV, the decay can be appreciably displaced from the primary vertex (depending also on the W_R mass), while for even lower m_N, the decay happen most of the time outside the detector, appearing as a missing energy signature. These regions are naturally overlapping, as we will show below. The displaced decay regime was studied in Ref. [26] for the LHC. For the FCC, the prospects and sensitivities for observing displaced vertices are strongly dependent on the inner detector design and vertexing challenges, so that, albeit very interesting, they are clearly premature. The missing energy signatures, on the other hand, are straightforward
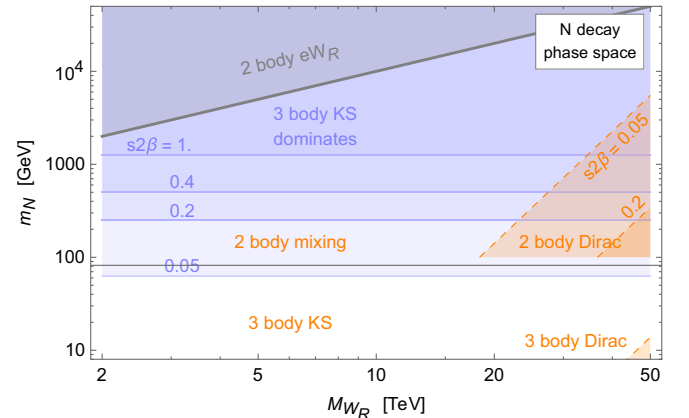

FIG. 5. Dominant N decay channels as a function of M_{W_R}, m_N and for various choices of t_β. The standard three-body KS decay dominates everywhere for $m_N < M_{W_R}$, except for m_N just above M_W, where N can decay to $W\ell$ depending on t_β via ξ_{LR}, and for very large M_{W_R}, where decays via the Dirac mass can be relevant.

and only weakly depend on the detector size. We will analyze them below.

III. BACKGROUNDS

Let us focus on the backgrounds for the cases in which N decays inside the detector (we discuss the missing energy background later on). Given the signature characteristics—namely, at least one highly energetic prompt lepton, low missing energy, and one or more jets—we identify the following possible SM processes contributing as backgrounds:

(1) W boson plus one or two jets.
(2) Drell-Yan $\ell^+\ell^-$ plus one or two jets.
(3) Diboson production VV with up to two jets.
(4) $t\bar{t}$ plus up to one jet.

For all of these SM backgrounds, we require the presence of at least one charged lepton. For example, in the VV samples, we force at least one of the bosons to decay leptonically.

All of the backgrounds are generated using MadGraph 3.3.2 and 2.8.0 [62], hadronized using PYTHIA 8 [63]. For detector simulation we used DELPHES 3 [64], adopting the provisional FCC card [65]. The parton level processes are generated at tree level with jet matching. In addition, a review of the literature for NLO and electroweak (EW) corrections brings the following k-factors:

(1) For w + 12j, NLO + EW corrections imply [66] a striking reduction of 50% or more, especially at high $p_T \gtrsim 10$ TeV as considered here, so we apply a 50% reduction.
(2) For DY + 12j, the NLO + γ-induced corrections also bring a reduction of up to 50%, so we adopt a correction of -30%.
(3) For vv + 012j, the NLO corrections lead to an enhancement of circa 1.5.
(4) For tt + 01j, NLO enhances by a factor of ~2.5 and EW corrections bring a reduction of 20%, so that an increase of 100% is a safe estimate.

At the same time, the signal is subject to a k-factor of 1.2–1.5 [15] for the range of W_R masses that we consider here. All of these estimates are clearly affected by their own uncertainties, motivating further studies for increasing the precision at 100 TeV.

As discussed above, after W_R decays, the prompt lepton and the subsequent leading jets typically carry high momentum on the order of $M_{W_R}/2$. On the other hand, backgrounds typically concentrate at lower p_T's, reaching at most a few TeV. For illustration, we plot the leading lepton p_T distributions in Fig. 6. As a result, the sensitivity to the signal can be efficiently improved by restricting the leading lepton and jet momenta to be of the order of TeV. At generator level, we require both a leading jet and a leading lepton to have $p_T > 1$ TeV, using the xptj and xptl parameters. This reduces the background cross sections
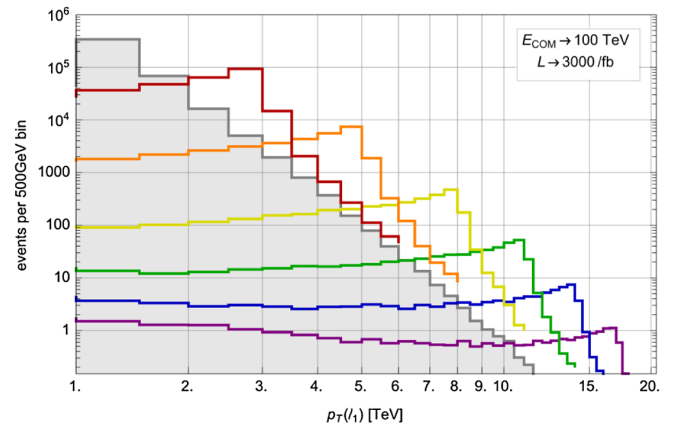

FIG. 6. Distribution of leading lepton p_T before cuts, for the background (gray) and various signal scenarios. $M_{W_R} = 6, 10, 16, 22, 28, 34$ TeV from left to right with a fixed $m_N = 1$ TeV.

substantially, so that enough statistics can be gathered by Monte Carlo, even for an integrated luminosity of 3/ab. The $\not{E} < 500$ GeV cut brings in a further reduction without significantly impacting the signal. Finally, we choose to impose even stronger cuts xptj, xptl > 1500 at the detector level, which further reduces the first backgrounds by 10, and the softer tt + 01j by more than 10^3.

The efficiency of the above cumulative cuts on the signal varies approximately from 40% at low $M_{W_R} \sim 7$ TeV to about 90% at highest $M_{W_R} \sim 40$ TeV (the signal is largely off shell and moves to softer p_T). The cut flow and final cross sections for the background are reported in Table. I. The most dominant process is w + 12j, and the other processes can be safely neglected in the present study.

As is evident from Fig. 6, if one wished to focus solely on the higher W_R masses at higher luminosity, then more stringent cuts could even be imposed from the beginning. This would further reduce the need for large samples in the

TABLE I. Table of background cross sections versus various cut requirements. All the cross sections are in pb, and the cuts are in GeV. For each case, the subprocesses with at least one final lepton were selected. For any jet or lepton, a minimal momentum is assumed, with ptj > 20, ptl > 10. At the analysis level, we impose even stronger cuts on the leading jet/lepton with xptj, xptl > 1500. The bold numbers correspond to the final cross section after all the subsequent cuts and after applying the k-factor.

Backgrounds [pb] ($\sqrt{s} = 100$ TeV)	w + 12j	DY + 12j	vv + 012j	tt + 01j
xptj, xptl > 50	5700	1000	180	480
xptj, xptl > 500	4.0	0.45	0.110	0.031
+xptl > 1000	0.46	0.030	0.017	0.0045
+misset < 500	0.39	0.030	0.011	0.0028
+xptj, xptl > 1500 (detector)	**0.047**	**0.0025**	**0.001**	**0.000012**
+k-factors	**0.023**	**0.0017**	**0.0015**	**0.000024**

generated background. We opt instead for very minimal cuts and a larger set of statistics, which should reliably simulate also the lower values of M_{W_R} (still above the reach of the LHC) and lower luminosities. To assess the sensitivity, we employ a cut-free method [26], as described in Sec. V.

IV. SIGNAL

The signal was simulated with the same settings and cuts as the background. We used the LRSM model file [67] at LO, which was introduced in Ref. [68] and updated from Ref. [60].

The single prompt lepton ℓ_1 from W_R decay is typically well isolated and can serve as a high efficiency trigger. At the same time, the N decay products are always very energetic, as shown in the previous sections. This naturally happens for light N ($m_N \ll M_{W_R}$), which is boosted and whose decay products typically have $p_T \sim M_{W_R}/3$. Likewise, the heavier N ($m_N \lesssim M_{W_R}$) features an energetic *secondary* lepton and jets that similarly have a large momentum $\sim m_N/3$.

At the detector level, due to isolation limitations, it is not always possible to separate all the N decay products, especially when they are boosted and produce a single jet that contains the secondary charged lepton ℓ_2. Our approach is thus to reconstruct the W_R invariant mass of the (leading) jet, together with one (leading) lepton, or possibly two leptons if they are isolated. The single-lepton-plus-jet variable $m_{\mathrm{inv}}(l_1 j_1)$ is more appropriate for the light (boosted) RH neutrino regime, while the two-lepton-plus-jet variable $m_{\mathrm{inv}}(l_1 l_2 j_1)$ is sensitive to the higher RH neutrino masses. We also always consider leptons and jets with a minimal $p_T(\ell) = 10$ GeV and $p_T(j) = 50$ GeV.

In Fig. 7, we plot the distribution of events in the $p_T(l_1) - m_{\mathrm{inv}}(l_1 j_1)$ plane, both for the background and for a selection of signal scenarios with fixed $m_N = 1$ TeV. As one can see, for increasing M_{W_R}, the signal peaks progressively outside of the background region. This is characteristic of s-channel resonance searches and is particularly promising.

Varying the RH neutrino mass leads to various distributions that are shown in Fig. 8. One can observe that, because the RH neutrino decays to a further lepton and jets, and because at detector level one cannot distinguish between leptons, it may happen that the secondary lepton from N decay is harder and takes the role of the first. This happens at large m_N masses, when $p_T(\ell_2) \simeq m_N/3 > p_T^{\max}(\ell_1)$ from Eq. (6). Solving for m_N, we find $m_N/M_{W_R} = (\sqrt{10} - 1)/3 \simeq 0.72$, with $p_T^{\max} \simeq M_{W_R}/4$. This applies to the rightmost frames in Fig. 8.

A similar distribution of events appears in the $p_T(l_1) - m_{\mathrm{inv}}(l_1 l_2 j_1)$ plane at large m_N masses. In the next section, we will take into account both channels and estimate the sentivity in the entire M_{W_R}-m_N plane.
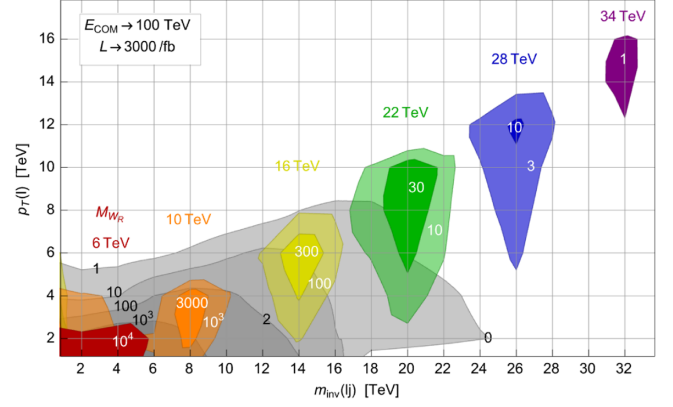

FIG. 7.   Distribution of events in 2×2 TeV bins in the space of the leading lepton $p_T(l_1)$ versus $m_{\mathrm{inv}}(l_1 j_1)$. The background is shown underneath in gray, and overlayed regions correspond to signal scenarios with $M_{W_R} = 6, 10, 16, 22, 28, 34$ TeV from left to right, and fixed $m_N = 1$ TeV (for clarity, only the highest contours are shown). The signal moves progressively to a background-free region as M_{W_R} becomes heavier.

V. SENSITIVITY

While a fair idea of the reach may be obtained from Fig. 6 with a sliding cut on $p_T(\ell)$ as a function of M_{W_R}, the further dependence on m_N makes this procedure unfeasible. A simpler and optimal method to assess the sensitivity for any choice of model parameters was devised in Ref. [26]. It consists of splitting the background and signal events in a multidimensional binning along a few relevant observables, and defining the overall sensitivity as the sum in quadrature of single bin sensitivities:

$$\Sigma^2 = \sum_{i \in \mathrm{bins}} \frac{s_i^2}{s_i + b_i}, \qquad (9)$$

where s_i and b_i are the expected numbers of signal and background events in each bin (see Fig. 7 for an example of a two-variable binning of signal and background). The method is quite robust with respect to binning variations, with a systematic uncertainty that can be suitably controlled. We refer to Ref. [26] for the illustration and the theoretical discussion of the method.

A. The KS and LJ signature

The binning grid in this case concerns three observables: $p_T(\ell)$, $m_{\mathrm{inv}}(\ell j)$, and $m_{\mathrm{inv}}(\ell\ell j)$, which are reported in the first column of Table II. Each of them spans the range (above the minimal cut) in bins of 2 TeV.

As discussed above, $p_T(\ell)$ is already a strong discriminator between the signal and background. The other two variables address the reconstruction of the M_{W_R} invariant mass, and are useful to boost the sensitivity in the low $[m_{\mathrm{inv}}(\ell j)]$ and heavy $[m_{\mathrm{inv}}(\ell\ell j)]$ RH neutrino mass regimes.
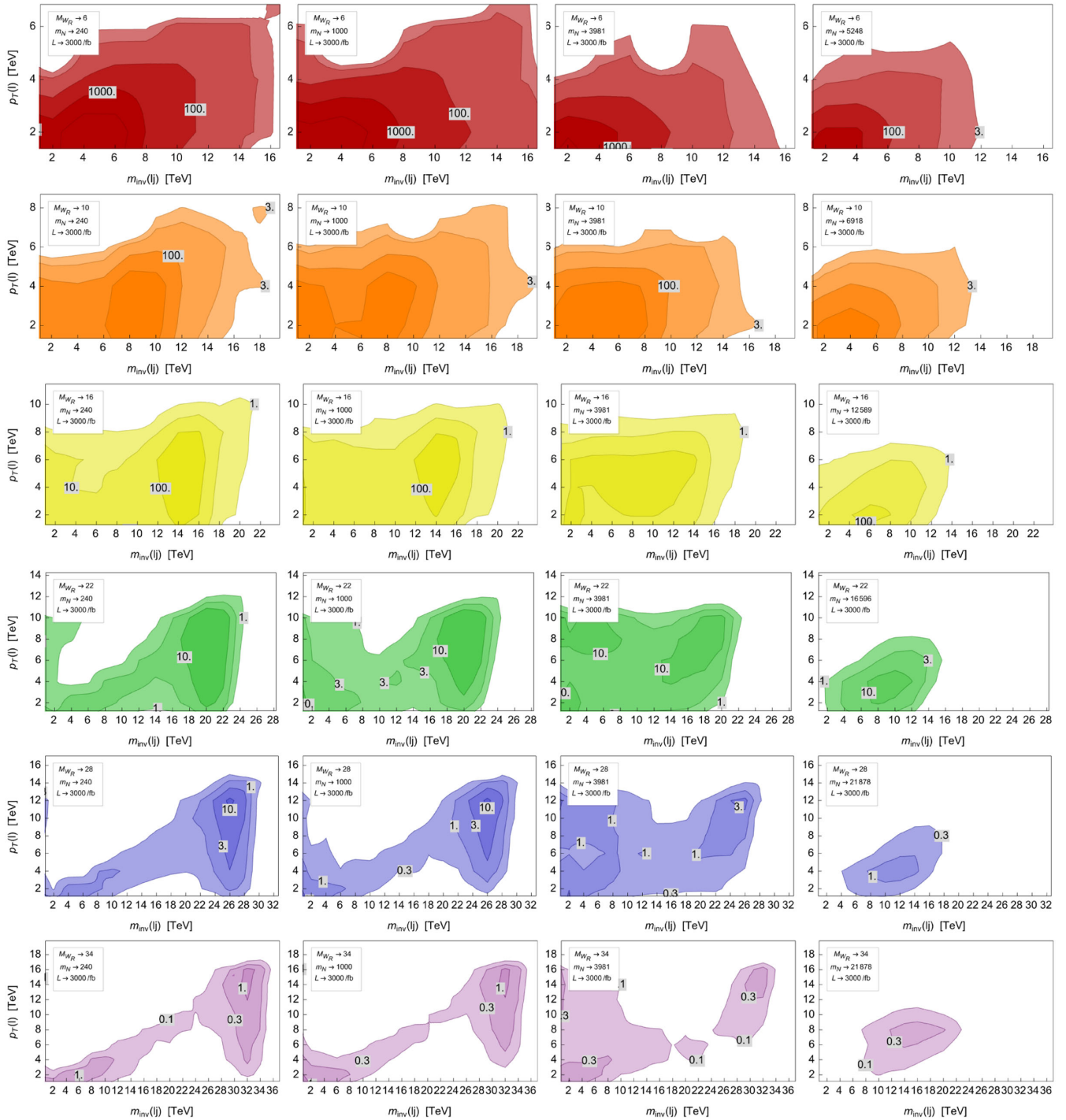
FIG. 8.   Distribution of leading lepton $p_T(l_1)$ versus $m_{\rm inv}(l_1 j_1)$ for various heavy neutrino masses and fixed M_{W_R}.

In Table II, we also report the resulting sensitivity for a selection of signal points in the M_{W_R}-m_N parameter space, where the successive table rows display the sensitivity obtained by adding in turn the corresponding variable to the binning. One can notice the increase in sensitivity in the second line in particular for light N, and the strong increase in the last line, especially for large N masses. In Fig. 9, we display the sensitivity in the

M_{W_R}-m_N plane for the separate channels where the final signature has LLJ (upper) or LJ (lower) only. One can appreciate the complementarity of the two channels for low and high RH neutrino masses. The final combined sensitivity is shown in Fig. 10 for an integrated luminosity of $L = 3/{\rm ab}$. It is quite notable that the combined reach of the two channels together is around $37/35/32$ TeV at confidence levels (CL's) of $2\sigma/3\sigma/5\sigma$.
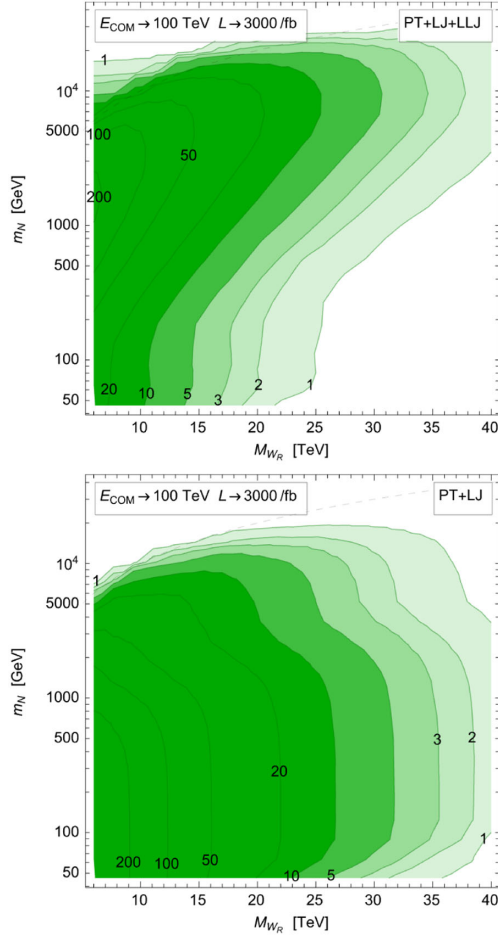
FIG. 9. Sensitivity (number of σ's) of the resolved two-lepton LLJ (upper) and single-lepton LJ (lower) channels.

Also, for an early run with a low integrated luminosity of $L = 30$ fb, the 5σ discovery reach is around 15 TeV.

At the lower end of $M_{W_R} \lesssim 15$ TeV, the FCC-hh can also probe the heavy $m_N > M_{W_R}$ regime, where W_R is produced off shell, but with a sufficiently large invariant mass to generate an N with mass up to $m_N \simeq 15$ TeV.

Figure 10 also shows the impact of the presence of t_β. For $m_N > M_W$, we see a depletion of the observed signal rate, as discussed in Sec. II C. On the other hand, the production via W opens up below M_W and leads to an increase. However, this happens in the light-N regime,

where N decay is progressively displaced. Therefore, the dependence on t_β would be of major interest in future studies of displaced decays at FCC-hh.

B. The missing energy signature

For light $m_N \lesssim 300$ GeV, the N decay length in the lab frame becomes long enough that the probability of it decaying outside of the detector becomes sizeable. Experimentally, this shows up as a prompt lepton plus missing energy, which is the signature usually assumed in searches for a sequential $W' \to \ell\nu$ [20].

For the FCC-hh, we assume a conservative detector size of 5 meters and calculate the expected number of those events where N decays entirely outside of the detector, while ℓ_1 always remains prompt. The technical details of this analytical calculation are described at the end of the Appendix. To compare with the estimated expected SM backgrounds, we separate the events into bins of transverse mass m_T, as considered in Refs. [20,69], but we rescale the cross sections to $\sqrt{s} = 100$ TeV. The background turns out to be dominated by single-W production and subdominant Drell-Yan, $t\bar{t}$, and multijet components.

The final result is shown as a shaded orange region and covers the lower part of Fig. 10. It demonstrates that in this channel, the $3\sigma(5\sigma)$ expected FCC reach extends up to $M_{W_R} \simeq 37(33)$ TeV and up to $m_N \simeq 300$ GeV. The sensitivity reach here is thus slightly higher than in the KS and LJ channels, as already happens at the LHC [26], but this shows a nice complementarity. The invisible channel reach estimate would be slightly reduced in the case where a much larger detector size is chosen, but this would be to the advantage of the other channels discussed above. In addition, the possibility of detecting displaced N decays, not yet considered at this stage, would boost the sensitivity of KS in the low-m_N regime, as argued in Ref. [26].

An important point concerns the connection between colliders and neutrinoless double beta decay ($0\nu\beta\beta$) in this light $m_N \lesssim 300$ GeV regime. There are a couple of new sources for the $0\nu\beta\beta$ rate present in the LRSM [6,70], in addition to the standard light Majorana neutrino exchange. While the standard double weak decay produces two outgoing electrons with *left* chirality, in the LRSM new diagrams appear with *two right* or *one left- and one*

TABLE II. The first column reports the chosen grid binning variables, their range, and the number of corresponding bins. The columns on the right correspond to sensitivities in σ obtained with $3/\text{ab}^{-1}$. Subsequent rows show the progression/optimization of the sensitivity after adding in turn each binning variable to the grid, and the bottom row represents our final sensitivity. The selection of points in the m_N-M_{W_R} parameter space for progressively larger m_N values ranges from the single lepton to the two isolated leptons regime.

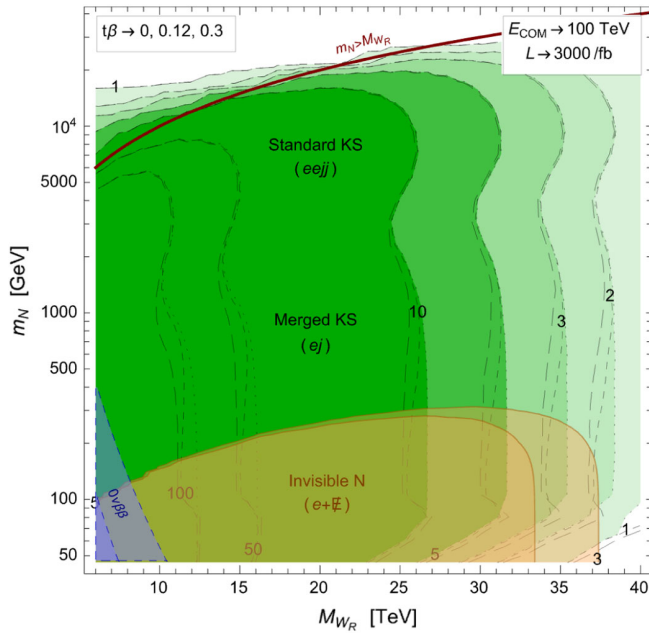| Variable	$\mathcal{L} = 3\text{ab}^{-1}$ Range	Bins	M_{W_R}: m_N:	10 240	10 1000	10 3981	10 9550	18 240	18 1000	18 3981	18 16596	32 240	32 1000	32 3981	32 28840
$p_T(\ell_1)$	$\{1.5, 31.5\}$ TeV	16		106	78.5	80.8	2.19	25.8	26.0	25.1	1.21	3.43	3.78	2.73	0.326
$m_{\text{inv}}(\ell_1 j_1)$	$\{1.5, 41.5\}$ TeV	20		123	89.7	86.9	2.99	29.5	28.2	26.2	1.61	4.06	4.28	3.25	0.531
$m_{\text{inv}}(\ell_1 \ell_2 j_1)$	$\{1.5, 41.5\}$ TeV	20		124	94.0	109.	15.7	29.4	28.6	29.6	6.03	4.05	4.32	3.60	0.992

FIG. 10.   The green areas show the final KS-plus-LJ sensitivity (in number of σ's) achievable with 3/ab integrated luminosity. We show also the dependences on $t_\beta = 0$, 0.12, 0.3 (dotted, dashed, long-dashed lines). The overlayed orange shaded region in the lower part of the frame displays the 3σ and 5σ sensitivities to the $\ell + \not{E}$ signature.

FIG. 11.   LRSM contribution to $0\nu\beta\beta$ from processes including the right-right heavy N exchange and the left-right amplitude via gauge boson mixing (for a benchmark value of $t_\beta = 0.3$). The red and blue shaded regions show the mass ranges saturating various $0\nu\beta\beta$ sensitivities, and their interplay with the invisible N channel at FCC in orange. The lower part of the diagram in shaded gray shows the exclusion from BBN.

righthanded outgoing electron. It turns out that the latter opposite-chirality process may be the increasingly dominant one for heavier M_{W_R}. It is mediated by the exchange of two W's, or by one W plus one W_R. The latter option has a suppressed nuclear matrix element (see Refs. [71–73] and [52] for details), and one is left with the double W exchange that can produce opposite-chirality electrons via the LR gauge boson mixing. This contribution is thus driven by the magnitude of t_β.

The sensitivity to $0\nu\beta\beta$ experiments is shown in Fig. 11 for a benchmark value of $t_\beta = 0.3$ with the calculable[1] seesaw Dirac mixing $U_{\nu N} \simeq (m_\nu/m_N)^{1/2}$. We depict the region where the LRSM can saturate the possible $0\nu\beta\beta$ evidence, for the present and future planned sensitivities (GERDA-II, $m_{ee} < 92$ meV; and LEGEND-1000, $m_{ee} < 9$–21 meV). One can see that the region extends up to the scale of $M_{W_R} \simeq 30$ TeV, with light N in the (sub-)GeV range. For $t_\beta = 0.12$, the region extends up to $M_{W_R} \sim$ 15 TeV. We also recall that $m_N < 0.14$–few GeV is excluded by the requirement that N decay fast enough in order not to spoil the BBN predictions [54,74]; see the gray shading. These limits come about because an N with such mass would be produced thermally in the early

Universe and then become long-lived with $\tau_N \gtrsim 1$ sec, and would therefore spoil BBN.

Finally, this region of parameter space harbors the possibility of having a (warm) dark matter (DM) candidate. Namely, for very light masses of N close to the keV scale, one can satisfy the DM abundance with entropy dilution [53,54]. Indeed, it has been argued in Ref. [54] that, by using the phase-space suppression for the dilutor lifetime and the drop of relativistic degrees of freedom in $g_*(T)$ around the QCD phase transition, an $\mathcal{O}(\text{TeV})$ solution for M_{W_R} may be attainable. This requires a very light m_N at about the keV scale, in line with constraints from dwarf spheroidals [75]. Without resorting to the g_* shift, a second solution for M_{W_R} exists in the 20 TeV range (see Fig. 6 of Ref. [54]), which goes further up for heavier DM candidates (see also Ref. [76] for the heavy-M_{W_R} scenarios).

Recently, it was argued that the possibility of having a DM candidate is subject to strong constraints from the large-scale structure data [55]. This happens because the secondary DM production from entropy injection spoils the matter power spectrum with potentially significant impact on the LR scale. The fate of the DM with low M_{W_R} remains to be established, but in any case, the interplay with future colliders lies precisely in connecting the DM thermal freeze-out to the missing energy signal at the FCC-hh.

Thus, in Fig. 11, one can appreciate the interplay between $0\nu\beta\beta$ and the invisible N channel at FCC: a positive $0\nu\beta\beta$

---

[1]The size of the mixing is predicted in LRSM via the calculable Dirac mass matrix [47,48], but it might be enhanced in small corners of parameter space [52].
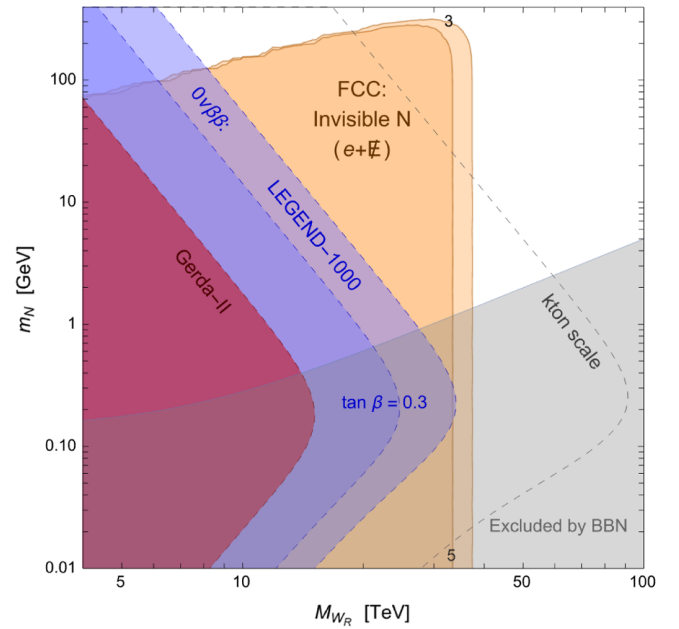
finding, in absence of the standard contribution (e.g., because of normal hierarchy; see the discussion in Ref. [77]), would imply an upper bound on M_{W_R} [74] that we estimate in the range of 10–30 TeV. This would constitute a case for looking for W_R and N at an FCC-hh. Further experiments at the kton scale are envisaged to push the $0\nu\beta\beta$ search down to an impressive ~ 1 meV [78]. These would connect to LRSM scales as high as $M_{W_R} \simeq 100$ TeV, even beyond the reach of a 100 TeV collider.

VI. OUTLOOK

While the quest for a theory of neutrino masses is still open, the LRSM stands as a unique candidate connecting their origin with an understanding of parity breaking in weak interactions. Ongoing experimental efforts are at the limit of their capabilities in probing the model parameter space. This is true for collider LHC probes, with an estimated reach of $M_{W_R} \simeq 7$ TeV [26], and also low-energy probes. Most notable are current and planned B-meson flavor observables that will be sensitive to mass scales at most up to $M_{W_R} \simeq 10$ TeV [34]. It is thus important to address the prospects with the planned and proposed future experiments, with the energy frontier being the elected arena to search for direct signs of new physics. In this work, we systematically estimated the reach of a hadronic (pp) FCC with a 100 TeV center-of-mass energy in the search for a W_R decaying leptonically, which has the potential to uncover lepton number violation, for diverse choices of M_{W_R} and m_N, and we took into account the LR gauge boson mixing.

We recalled the different signatures emerging as a function of the mass of the RH neutrino N: (i) $\ell\ell jj$ in the KS process for $M_{W_R} \gtrsim m_N \gtrsim 1$ TeV, (ii) ℓj_N in the case when the N decay products are merged in a single fat jet for few TeV $\gtrsim m_N \gtrsim 100$ GeV, and (iii) the $\ell + \not{E}$ signature when N decays outside the detector for $m_N < 300$ GeV. All these channels feature at least one prompt high-p_T lepton, which ensures triggering and allows us to reduce the expected SM background by many orders of magnitude. It turns out that by requiring a minimal p_T of the order of 1.5 TeV, the background is dominated by `w + jets` and could be simulated to satisfactory high statistics. We showed indeed that, as expected, the background and signal live in different regions of kinematic observables, thus effectively leaving just the signal at high energies. As a result, the reach is mainly limited by the center-of-mass energy, luminosity, and quark PDFs.

We thus assessed the exclusion reach by adopting a unified binned likelihood approach [26], which does not require sliding windows as a function of model parameter choices. The results were presented in Fig. 10. For the KS and merged regions [(i) and (ii)], we estimated a reach for M_{W_R} as high as 35 TeV at a 3σ CL, for an integrated luminosity of 3/ab. This is similar to the reach expected for the simpler $W_R \to jj$ channel.

It is worth recalling here that within region (ii), in the lightest N regime of $m_N \sim 100$–300 GeV, the RH neutrino can decay at an appreciable distance, giving rise to a *displaced jet* [26]. Its study will be very interesting as soon as definite detector geometry and sensitivities become available.

Still, this case overlaps with the even lower m_N regime [case (iii)] where N decays outside the detector and appears as missing energy, thus matching with the search for $W' \to \ell\nu$. We estimated that the 3σ sensitivity covers a region extending up to $M_{W_R} \simeq 37$ TeV and up to $m_N \simeq 300$ GeV.

This region features an interesting connection with $0\nu\beta\beta$ contributions from the LRSM, especially in light of current, planned, and envisioned experiments. Figure 11 reports this interplay, showing that a possible signal at forthcoming and future $0\nu\beta\beta$ probes, in the absence of the standard neutrino mass mechanism, would imply a M_{W_R} below ~ 30 TeV and a m_N below ~ 100 GeV, which overlaps precisely with the invisible N decay at FCC here considered. Incidentally, cosmology presents an interesting interplay, either as a constraint from BBN or as an opportunity for having a warm DM candidate.

APPENDIX: DRELL-YAN W_R AND N PRODUCTION AND DECAY RATES

In this appendix, we review in detail the production of W_R and its decays into the ℓN final state (on shell and $2 \to 2$).

1. Resonance production

The amplitude for the production of an on-shell resonance $q(p_1)q(p_2) \to V(P)$ at parton level is

$$\mathcal{A} = ig\bar{v}_1\gamma^\mu(v_q + a_q\gamma_5)u_2\varepsilon_\mu^{(\lambda)}. \tag{A1}$$

Averaging over initial spins, including the color factor and summing over polarizations λ, we have

$$\begin{aligned}
|\mathcal{M}|^2 &= \frac{N_c}{4}g^2\sum_\lambda \varepsilon_\mu^{(\lambda)}\varepsilon_\nu^{(\lambda)*}\text{tr}(\gamma^\alpha\gamma^\mu\gamma^\beta\gamma^\nu(v_q + a_q\gamma_5))p_{1\alpha}p_{2\beta} \\
&= \frac{N_c}{4}g^2\left(-g_{\mu\nu} + \frac{(p_1+p_2)_\mu(p_1+p_2)_\nu}{M^2}\right) \\
&\quad \times 4(p_1^\mu p_2^\nu + p_1^\nu p_2^\mu - g^{\mu\nu}p_1p_2)(v_q^2 + a_q^2) \\
&= N_c g^2 \hat{s}(v_q^2 + a_q^2), \tag{A2}
\end{aligned}$$

where $\hat{s} = (p_1 + p_2)^2 = 2p_1 p_2$. The differential cross section is

$$d\hat{\sigma} = (2\pi)^4 \frac{|\mathcal{M}|^2}{2\hat{s}} d\varphi, \tag{A3}$$

such that integration over the final-state momentum gives

$$\hat{\sigma} = \frac{\pi|\mathcal{M}|^2}{\hat{s}} \delta(\hat{s} - M^2) = 4N_c \pi^2 \alpha_2 (v_q^2 + a_q^2) \delta(\hat{s} - M^2). \tag{A4}$$

For the W_R cross section, we substitute $g \to gV_{ij}/\sqrt{2}$, $v_q = a_q = 1/2$ and obtain

$$\hat{\sigma}_{q_i \overline{q_j} \to W_R} = N_c \pi^2 \alpha_2 |V_{ij}|^2 \delta(\hat{s} - M_{W_R}^2). \tag{A5}$$

Approximating the δ function with the Breit-Wigner resonance

$$\pi\delta(\hat{s} - M^2) \simeq \frac{\Gamma M}{(\hat{s} - M^2)^2 + (\Gamma M)^2}, \tag{A6}$$

we get the parton level cross section

$$\hat{\sigma}_{q_i \overline{q_j} \to W_R} = N_c \pi \alpha_2 |V_{ij}|^2 \frac{\Gamma_{W_R} M_{W_R}}{(\hat{s} - M_{W_R}^2)^2 + (\Gamma_{W_R} M_{W_R})^2}. \tag{A7}$$

a. Proton-proton

To obtain the pp cross section, the partonic $\hat{\sigma}$ is convoluted with the PDFs. There is an additional $1/N_c^2$ combinatorial factor for the color connection,

$$\frac{d^2\sigma_{pp \to W_R^+}}{dx_1 dx_2} = \frac{\pi^2 \alpha_2}{N_c} \sum_{u,d} |V_{ud}|^2 (f_u(x_1) f_{\overline{d}}(x_2) + 1 \leftrightarrow 2)$$
$$\times \delta(\hat{s} - M_{W_R}^2). \tag{A8}$$

To integrate over $\hat{s}$, we change integration variables from $x_{1,2}$ to the rapidity y of W_R and the partonic center-of-mass energy $\hat{s}$. The proton mass is small and quarks are nearly massless; therefore,

$$\hat{s} = (p_1 + p_2)^2 = 2p_1 p_2 = 2x_1 x_2 P_1 P_2 = x_1 x_2 s. \tag{A9}$$

Moreover, proton beams are symmetric and energetic, such that the W_R momentum is

$$P_W^{0,3} = x_1 P_1^{0,3} + x_2 P_2^{0,3} = \frac{\sqrt{s}}{2}(x_1 \pm x_2). \tag{A10}$$

This setup gives the W_R rapidity

$$y \equiv \frac{1}{2} \ln\left(\frac{P_W^0 - P_W^3}{P_W^0 + P_W^3}\right) = \frac{1}{2} \ln\left(\frac{x_2}{x_1}\right). \tag{A11}$$

When W_R is produced at rest, we have $P_W^3 = 0 = \sqrt{s}(x_1 - x_2)/2$, which implies $x_1 = x_2$ and $y = 0$. The product of x_1 and x_2 is fixed by the on-shell condition for W_R, which gives $P_W^{02} - P_W^{32} = M_{W_R}^2 = x_1 x_2 s$. Now, the maximum value of $x_2^{\max} = 1$ corresponds to $x_1^{\min} = M_{W_R}^2/s$, and the maximal rapidity is

$$y_{\max} = \ln\left(\frac{\sqrt{s}}{M_{W_R}}\right). \tag{A12}$$

This also corresponds to the situation when W_R is maximally boosted:

$$\gamma_R^{\max} = \frac{P_W^0}{M_{W_R}} = \frac{\sqrt{s}}{2}(x_1^{\min} + x_2^{\max})$$
$$= \frac{1}{2}\left(\frac{\sqrt{s}}{M_{W_R}} + 1\right) \simeq \frac{\sqrt{s}}{2M_{W_R}}, \tag{A13}$$

where the last approximation is valid when $\sqrt{s} \gg M_{W_R}$. Because quarks and protons are nearly massless, the $x_{1,2}$ have symmetric limits and $y_{\min} = -y_{\max}$. We change variables using the Jacobian

$$dx_1 dx_2 = \frac{d\hat{s}dy}{s} = x_1 x_2 \frac{d\hat{s}dy}{\hat{s}}, \tag{A14}$$

and we finally end up with

$$\frac{d\sigma}{dy} = \frac{\pi^2 \alpha_2}{N_c M_{W_R}^2} \sum_{u,d} |V_{ud}|^2 (x_1 f_u(x_1) x_2 f_{\overline{d}}(x_2) + 1 \leftrightarrow 2). \tag{A15}$$

Both partonic fractions $x_{1,2}$ are given by the collision energy and W_R rapidity $x_{1,2} = M_{W_R} e^{\pm y}/\sqrt{s}$. The distributions in y are symmetric at the LHC and extend to $\pm y_{\max}$.

2. Resonance decays

The on-shell W_R resonance can decay in different ways. The dominant decay rates are

$$\Gamma\left(W_R \to q_R \overline{q'_R}\right) = \frac{\alpha_2}{8} M_{W_R}(4 + (2 + x_t)(1 - x_t)^2), \tag{A16}$$

$$\Gamma(W_R \to \ell_R N) = \frac{\alpha_2}{24} |V_{\ell N}|^2 M_{W_R}(2 + x_N)(1 - x_N)^2, \tag{A17}$$

where $x_f = 1 - m_f^2/M_{W_R}^2$, CKM is unitary, and $V_{tb} \sim 1$. Once we turn on the gauge boson mixing ξ_{LR} in Eq. (1), the decay modes of WZ and Wh, as well as the SM W decays to $\ell_R N$, open up. They proceed with the following rates:

$$\Gamma(W_R \to WZ) = \Gamma(W_R \to Wh) = \frac{\alpha_2}{48} s_{2\beta}^2 M_{W_R}, \quad \text{(A18)}$$

$$\Gamma(W \to \ell_R N) = \xi_{LR}^2 \frac{\alpha_2}{24} |V_{\ell N}|^2 M_W (2 + x_N)(1 - x_N)^2. \tag{A19}$$

At the same time, the dominant rates in Eqs. (A16) and (A17) get negligibly suppressed by $1 - \xi_{LR}^2$.

3. ℓN fermion pair production via resonance

Instead of the $2 \to 1$ resonance production above, we can consider the direct $2 \to 2$ scattering of $pp \to \ell N$ via the W_R propagator. The scattering amplitude in the unitary gauge is given by

$$\mathcal{A} = i\frac{g}{\sqrt{2}} V_{ij} \bar{u}_{1R} \gamma^\mu u_{2R} \frac{-ig_{\mu\nu}}{\hat{s} - M^2 + i\Gamma M} i\frac{g}{\sqrt{2}} V_{\ell N} \bar{u}_{3R} \gamma^\nu u_{4R}$$

$$= \frac{i}{2} \frac{g^2 V_{ij} V_{\ell N}}{\hat{s} - M^2 + i\Gamma M} (\bar{u}_{1R} \gamma^\mu u_{2R})(\bar{u}_{3R} \gamma_\mu u_{4R}), \tag{A20}$$

where the momentum part of the W_R propagator vanishes, because we take quarks to be massless. Turning on the gauge boson mixing ξ_{LR} does not modify the production much; the $\bar{u}_{1R} \gamma^\mu u_{2R}$ term goes into $\cos(\xi_{LR}) \bar{u}_{1R} \gamma^\mu u_{2R} + \sin(\xi_{LR}) \bar{u}_{1L} \gamma^\mu u_{2L}$. After squaring the amplitude and summing over the spins, we get $\cos(\xi_{LR})^2 + \sin(\xi_{LR})^2 = 1$, because the R and L terms sum into the same expression; moreover, the RL interference term vanishes in the limit of zero quark masses. The spin-averaged amplitude is

$$\overline{|\mathcal{M}|^2} = \frac{1}{16} N_c g^4 \frac{|V_{ij} V_{\ell N}|^2}{(\hat{s} - M^2)^2 + (\Gamma M)^2} \text{tr}\left(\not{p}_1 \gamma^\mu \not{p}_2 \gamma^\nu P_R\right)$$

$$\times \text{tr}\left(\not{p}_3 \gamma_\mu \not{p}_4 \gamma_\nu P_R\right), \tag{A21}$$

$$= 4N_c \alpha_2^2 \pi^2 \frac{|V_{ij} V_{\ell N}|^2}{(\hat{s} - M^2)^2 + (\Gamma M)^2} \hat{t}(\hat{t} - m^2), \tag{A22}$$

where $\hat{t} = (p_1 - p_3)^2 = (p_2 - p_4)^2$. The partonic cross section is then

$$\hat{\sigma}_{q_i \bar{q}_j \to W_R^* \to \ell N} = \frac{1}{16\pi\hat{s}^2} \int_{m^2 - \hat{s}}^0 \overline{|\mathcal{M}|^2} d\hat{t} \tag{A23}$$

$$= \frac{1}{16\pi\hat{s}^2} 4N_c \alpha_2^2 \pi^2 \frac{|V_{ij} V_{\ell N}|^2}{(\hat{s} - M^2)^2 + (\Gamma M)^2} \frac{1}{6}$$

$$\times (\hat{s} - m^2)^2 (2\hat{s} + m^2) \tag{A24}$$

$$= N_c \pi \alpha_2 |V_{ij}|^2 \frac{\sqrt{\hat{s}}}{(\hat{s} - M^2)^2 + (\Gamma M)^2} \frac{\alpha_2}{24} |V_{\ell N}|^2 \sqrt{\hat{s}}$$

$$\times \left(1 - \frac{m^2}{\hat{s}}\right)^2 \left(2 + \frac{m^2}{\hat{s}}\right). \tag{A25}$$

In the narrow-width limit and expanding near the pole $\hat{s} \simeq M^2$, the cross section becomes

$$\hat{\sigma}_{q_i \bar{q}_j \to \ell N} = N_c \pi \alpha_2 |V_{ij}|^2 \frac{\Gamma M}{(\hat{s} - M^2)^2 + (\Gamma M)^2}$$

$$\times \frac{\frac{\alpha_2}{24} |V_{\ell N}|^2 M (1 - \frac{m^2}{M^2})^2 (2 + \frac{m^2}{M^2})}{\Gamma} \tag{A26}$$

$$\simeq N_c \pi \alpha_2 |V_{ij}|^2 \pi \delta(\hat{s} - M^2) \frac{\Gamma_{W_R \to \ell N}}{\Gamma}$$

$$= \hat{\sigma}_{q_i \bar{q}_j \to W_R} \text{Br}_{W_R \to \ell N}. \tag{A27}$$

a. Proton-proton

The partonic cross section in Eq. (A23) is convoluted with the PDFs. The differential cross section is

$$\frac{d^2\sigma_{pp \to \ell^+ N}}{dx_1 dx_2} = \frac{\pi \alpha_2^2}{24N_c} \frac{\hat{s}}{(\hat{s} - M^2)^2 + (\Gamma M)^2}$$

$$\times \left(1 - \frac{m^2}{\hat{s}}\right)^2 \left(2 + \frac{m^2}{\hat{s}}\right)$$

$$\times \sum_{ud} |V_{ud} V_{\ell N}|^2 (f_u(x_1) f_{\bar{d}}(x_2) + 1 \leftrightarrow 2), \tag{A28}$$

and we integrate over the $x_{1,2}$ to get the total cross section:

$$\sigma_{pp \to \ell^+ N} = \int_{\frac{m^2}{s}}^1 dx_1 \int_{\frac{m^2}{x_1 s}}^1 dx_2 \frac{d^2\sigma_{pp \to \ell^+ N}}{dx_1 dx_2}. \tag{A29}$$

The final-state kinematic variables p_T^2 and η_ℓ, η_N constrain the integration regions. Let

$$p_1 = x_1 \frac{\sqrt{s}}{2}(1, 0, 0, 1),$$

$$p_3 = (m_T \cosh \eta_N, 0, p_T, m_T \sinh \eta_N), \tag{A30}$$

$$p_2 = x_2 \frac{\sqrt{s}}{2}(1, 0, 0, -1),$$

$$p_4 = (p_T \cosh \eta_\ell, 0, -p_T, -p_T \sinh \eta_\ell), \tag{A31}$$

where the transverse mass is defined by $m_T^2 = m^2 + p_T^2$. At high-momentum transfers considered here, the proton and charged lepton masses are negligible and $p_1^2 = p_2^2 = p_4^2 = 0$. However, we treat the heavy Majorana

neutrino as massive, with a mass $p_3^2 = m^2$. From these, we get the $x_{1,2}$ and the Mandelstam invariants, $\hat{t} = (p_1 - p_3)^2$ and $\hat{s} = (p_1 + p_2)^2$, to be

$$x_{1,2} = \frac{1}{\sqrt{s}} (m_T e^{\pm\eta_N} + p_T e^{\mp\eta_\ell}),$$

$$\hat{t} = -p_T(p_T + m_T e^{-\eta_{N\ell}}), \qquad \hat{s} = x_1 x_2 s, \qquad (A32)$$

where $\eta_{N\ell} = \eta_N + \eta_\ell$. The p_T and rapidities are functions of $x_{1,2}$ (s if fixed) and $\hat{t}$:

$$p_T^2 = \frac{-\hat{t}(\hat{t} + \hat{s} - m^2)}{\hat{s}}, \qquad e^{2\eta_N} = -\frac{x_1}{x_2}\left(1 + \frac{\hat{s}}{\hat{t}}\right),$$

$$e^{2\eta_\ell} = -\frac{x_2}{x_1}\left(1 + \frac{\hat{s}}{\hat{t} - m^2}\right), \qquad (A33)$$

$$= \frac{-\hat{t}(\hat{t} + \tau s - m^2)}{\tau s}, \qquad = -\frac{1}{\rho}\left(1 + \frac{\tau s}{\hat{t}}\right),$$

$$= -\rho\left(1 + \frac{\tau s}{\hat{t} - m^2}\right), \qquad (A34)$$

where we introduce

$$\tau = x_1 x_2, \qquad \rho = \frac{x_2}{x_1}. \qquad (A35)$$

The τ variable is useful because it corresponds to the invariant mass of the ℓN pair—namely, $m_{\rm inv}^2(\ell N) = (p_3 + p_4)^2 = \hat{s} = x_1 x_2 s = \tau s$. These variables simplify the imposition of cuts and efficiencies. From the matrix element in Eq. (A21) and the definition of the cross section in Eq. (A23), we have

$$\frac{d^3\sigma_{pp\to\ell^+ N}}{dx_1 dx_2 d\hat{t}} = \frac{\pi\alpha_2^2}{12\hat{s}^2} \frac{\hat{t}(\hat{t} - m^2)}{(\hat{s} - M^2)^2 + (\Gamma M)^2} \sum_{ud} |V_{ud} V_{\ell N}|^2 (f_u(x_1) f_{\bar{d}}(x_2) + 1 \leftrightarrow 2). \qquad (A36)$$

b. Invariant mass

The $m_{\rm inv} \in [m, \sqrt{s}]$. Taking into account that $m_{\rm inv}^2 = \hat{s} = x_1 x_2 s = \tau s$, we get that

$$\frac{d\sigma_{pp\to\ell^+ N}}{dm_{\rm inv}} = \frac{d\sigma_{pp\to\ell^+ N}}{dm_{\rm inv}^2} \frac{dm_{\rm inv}^2}{dm_{\rm inv}} = \frac{1}{s} \frac{d\sigma_{pp\to\ell^+ N}}{d\tau} 2m_{\rm inv} = \frac{2m_{\rm inv}}{s} \int_{m_{\rm inv}^2/s}^1 \frac{dx_1}{x_1} \frac{d^2\sigma_{pp\to\ell^+ N}}{dx_1 dx_2} \qquad (A37)$$

$$= \frac{\pi\alpha_2^2}{12 N_c s} \frac{m_{\rm inv}^3}{(m_{\rm inv}^2 - M^2)^2 + (\Gamma M)^2} \left(1 - \frac{m^2}{m_{\rm inv}^2}\right)^2 \left(2 + \frac{m^2}{m_{\rm inv}^2}\right)$$

$$\times \sum_{ud} |V_{ud} V_{\ell N}|^2 \int_{m_{\rm inv}^2/s}^1 \frac{dx_1}{x_1} (f_u(x_1) f_{\bar{d}}(x_2) + 1 \leftrightarrow 2), \qquad (A38)$$

where $x_2 = m_{\rm inv}^2/(x_1 s)$, and the Jacobian from $(x_1, x_2) \to (x_1, \tau)$ is equal to $1/x_1$.

c. Transverse momentum

Along the same lines, the p_T distribution is obtained by the chain rule

$$\frac{d\sigma_{pp\to\ell^+ N}}{dp_T} = \int_{x_{1,2}} \frac{d^3\sigma_{pp\to\ell^+ N}}{dx_1 dx_2 d\hat{t}} \frac{d\hat{t}}{dp_T}, \qquad (A39)$$

$$\frac{d\hat{t}}{dp_T} = \frac{2p_T\hat{s}}{\sqrt{(\hat{s} - m^2)^2 - 4p_T^2\hat{s}}}, \qquad (A40)$$

$$\hat{t}(\hat{t} - m^2) = \frac{\hat{s}}{2}(\hat{s} - m^2 - 2p_T^2 + \sqrt{(\hat{s} - m^2)^2 - 4p_T^2\hat{s}}). \qquad (A41)$$

This gives us the distribution over p_T, shown in Fig. 3. For $\hat{t} \in \mathbb{R}$, the argument of the square root in Eq. (A41) needs to be positive, which leads to an upper bound on p_T:

$$p_T \in \left[0, \frac{s - m^2}{2\sqrt{s}}\right]. \qquad (A42)$$

Furthermore, at a fixed value of p_T, the lower bound for $\tau = x_1 x_2$ is given by

$$\tau_0 = \frac{m^2 + 2p_T^2 + 2\sqrt{p_T^2(m^2 + p_T^2)}}{s} \xrightarrow{p_T \to 0} \frac{m^2}{s}, \qquad (A43)$$

and the integration limits in Eq. (A39) are given by

$$\int_{x_{1,2}} = \int_{\tau_0}^1 dx_1 \int_{\tau_0/x_1}^1 dx_2. \qquad (A44)$$

d. Invariant mass vs p_T

Likewise, we can get the double differential distribution over p_T and m_{inv} by combining the two chain rules and integrating over x_1:

$$\frac{d^2\sigma_{pp\to\ell^+N}}{dp_T dm_{\text{inv}}} = \frac{2m_{\text{inv}}}{s}\int_{m_{\text{inv}}^2/s}^1 \frac{dx_1}{x_1}\frac{d^3\sigma_{pp\to\ell^+N}}{dx_1 dx_2 d\hat{t}}\frac{d\hat{t}}{dp_T}, \quad (A45)$$

using Eqs. (A36), (A40), and (A41), where again $\hat{s} = m_{\text{inv}}^2$ and $x_2 = m_{\text{inv}}^2/(x_1 s)$. From Eq. (A40), we see that

$$p_T \in \left[0, \frac{m_{\text{inv}}^2 - m^2}{2m_{\text{inv}}}\right], \qquad \text{for a fixed } m_{\text{inv}} \in [m, s].$$

$$(A46)$$

The contours of the double differential cross section are interesting, in that they are dominated by a narrow diagonal line relative to off-shell W_R production, and some broader regions with lower p_T but fixed $m_{\text{inv}} \simeq M_{W_R}$, corresponding to on-shell W_R.

e. No cuts

Without cuts, the lower bound on τ is simply $\tau_0 = m^2/s$, as needed to produce a massive N. However, the integration limits for ρ are split into two regions:

$$\tau \in [\tau_0, \rho], \quad \text{when } \rho \in [\tau_0, 1] \quad \text{and} \quad \tau \in [\tau_0, 1/\rho]$$

for $\rho \in [1, 1/\tau_0]$. $\qquad (A47)$

Meanwhile, $\hat{t} \in [m^2 - \tau s, 0]$.

f. p_T cut

$p_T > p_{Tc}$ can be implemented within the integration limits. Note that $\eta_{\ell N}$ does not depend on p_T. From the p_T equation in Eq. (A34), we have

$$\hat{t}_{\pm}(\tau) = \frac{s}{2}(\tau_0 - \tau)\left(1 \pm \sqrt{1 - \frac{p_{Tc}^2}{s}\frac{4\tau}{(\tau_0 - \tau)^2}}\right), \quad (A48)$$

and from the positivity of the square root, a ρ-independent constant lower bound,

$$\tau_- = \tau_0 + \frac{2p_{Tc}^2}{s}\left(1 + \sqrt{1 + \frac{m^2}{p_{Tc}^2}}\right) \xrightarrow{p_{Tc}\to 0} \tau_0, \quad (A49)$$

appears. The $\tau - \rho$ integration plane is $\tau \in [\tau_-, \rho]$, when $\rho \in [\tau_-, 1]$ and $\tau \in [\tau_-, 1/\rho]$ for $\rho \in [1, 1/\tau_-]$.

g. η_ℓ cut

The restriction $|\eta_\ell| > \eta_{\ell c}$ makes the τ_- limit ρ dependent. Notice that $\hat{t}_{\text{min}} = 0$, so setting $\hat{t} = 0$,

$$\tau_-(\rho) = \tau_0\left(1 + \frac{e^{-2\eta_{\ell c}}}{\rho}\right) \xrightarrow{\eta_{\ell c}\to\infty} \tau_0, \quad (A50)$$

while the ρ interval comes from $\tau_-(\rho_-) = \rho_-$, and $\tau_-(1/\rho_+) = 1/\rho_+$, such that

$$\rho \in [\rho_-, \rho_+] = \left[\frac{\tau_0}{2}\left(1 + \sqrt{1 + \frac{4e^{-2\eta_{\ell c}}}{\tau_0}}\right), \frac{1}{\tau_0} - e^{-2\eta_{\ell c}}\right].$$

$$(A51)$$

Finally, the bound on $\hat{t}$ coming from Eq. (A34) is

$$\hat{t}(\tau) = s\left(\tau_0 - \frac{\tau}{1 + e^{-2\eta_{\ell c}}/\rho}\right),$$

$$-\hat{t}_{\text{max}} = -\hat{t}(\rho = 1) = s\left(\tau_0 - \frac{1}{1 + e^{-2\eta_{\ell c}}}\right). \quad (A52)$$

h. p_T and η_ℓ

With both cuts acting simultaneously, the integration limits become more complex. The upper bound on $\tau(\rho)$ remains the same; however, the lower bound τ_- depends on both p_T and η_ℓ cuts. More importantly, the ρ interval changes, as well as the limits on $\hat{t}$.

Let us start with the lower bound on τ. Solving the quadratic equation for $\hat{t}$ in Eq. (A34) and plugging into η_ℓ, we have

$$\tau_-^{\pm}(\rho) = (m^2 + p_{Tc}^2)\left(1 + \frac{e^{\pm 2\eta_{\ell c}}}{\rho}\right) + p_{Tc}^2(1 + e^{\mp 2\eta_{\ell c}}\rho).$$

$$(A53)$$

The $+(-)$ applies to regions of ρ above (below) 1, where the upper bound is $\rho(1/\rho)$, such that

$$\rho_+^b = -\frac{e^{\eta_{\ell c}}}{2p_{Tc}^2}\left(e^{\eta_{\ell c}}(m^2 + 2p_{Tc}^2) + \sqrt{e^{2\eta_{\ell c}}m^4 + 4p_{Tc}^2 s}\right),$$

$$(A54)$$

$$\rho_-^b = -\frac{e^{-\eta_{\ell c}}}{2(p_{Tc}^2 e^{2\eta_{\ell c}} - s)}\left(e^{\eta_{\ell c}}(m^2 + 2p_{Tc}^2) + \sqrt{e^{2\eta_{\ell c}}m^4 + 4(p_{Tc}^2 + m^2)s}\right). \quad (A55)$$

The lower bound in Eq. (A53) should not go below the ρ-independent one in Eq. (A49), which happens at

$$\rho_{\pm}^c = e^{\pm\eta_{\ell c}}\sqrt{1 + \frac{m^2}{p_{Tc}^2}}. \quad (A56)$$

Notice that above a limiting p_T cut

$$p_{Tc}^{2\,\text{lim}} = e^{-2\eta_{\ell c}}s - m^2, \quad (A57)$$

the η_ℓ cut becomes ineffective (we are back to the p_T-cut case above), and Eq. (A57) implies an upper limit on $\eta_{\ell c}^{\lim} = -\log(m/\sqrt{s})$.

i. N as missing energy

Let us compute the number of events $n_{\ell\not{E}}$, when N decays outside of the detector of size $l_0 \sim 5$ m. Events are distributed by an exponential distribution

$$\frac{\mathrm{d}n}{\mathrm{d}l} = n_0 \frac{\exp(-l/L)}{L},$$

$$L = \gamma_N \beta_N \tau_N = \frac{p_T}{m\Gamma_N}\sqrt{1 + \left(1 + \frac{m^2}{p_T^2}\right)\sinh\eta_N^2}, \quad (A58)$$

and the total number of events is obtained by integrating from ℓ_0 to ∞:

$$n_{\ell\not{E}} = \int_{l_0}^\infty \frac{\mathrm{d}n}{\mathrm{d}l}\mathrm{d}l = \mathcal{L} \iiint \frac{\mathrm{d}\rho\mathrm{d}\tau\mathrm{d}\hat{t}}{2\rho}\varepsilon_\ell(p_T, \eta_\ell)$$
$$\times \left(\frac{\mathrm{d}^3\sigma_{pp\to\ell N}}{\mathrm{d}\tau\mathrm{d}\rho\mathrm{d}\hat{t}}\right)e^{-l_0/L}, \quad (A59)$$

where $\mathcal{L}$ is the total luminosity and ε_ℓ is the charged lepton selection efficiency. Efficiencies may also include more stringent p_T and η_ℓ cuts.

[1] J. C. Pati and A. Salam, Lepton number as the fourth color, Phys. Rev. D **10**, 275 (1974); **11**, 703(E) (1975).

[2] R. N. Mohapatra and J. C. Pati, Left-right gauge symmetry and an isoconjugate Model of *CP* violation, Phys. Rev. D **11**, 566 (1975).

[3] G. Senjanović and R. N. Mohapatra, Exact left-right symmetry and spontaneous violation of parity, Phys. Rev. D **12**, 1502 (1975).

[4] G. Senjanović, Spontaneous breakdown of parity in a class of gauge theories, Nucl. Phys. **B153**, 334 (1979).

[5] P. Minkowski, $\mu \to e\gamma$ at a rate of one out of 10^9 muon decays? Phys. Lett. **67B**, 421 (1977).

[6] R. N. Mohapatra and G. Senjanović, Neutrino Mass and Spontaneous Parity Nonconservation, Phys. Rev. Lett. **44**, 912 (1980).

[7] T. Yanagida, Horizontal gauge symmetry and masses of neutrinos, Conf. Proc. C. **7902131**, 95 (1979).

[8] S. L. Glashow, The future of elementary particle physics, NATO Sci. Ser. B **61**, 687 (1980).

[9] M. Gell-Mann, P. Ramond, and R. Slansky, Complex spinors and unified theories, Conf. Proc. C **790927**, 315 (1979).

[10] W.-Y. Keung and G. Senjanović, Majorana Neutrinos and the Production of the Right-handed Charged Gauge Boson, Phys. Rev. Lett. **50**, 1427 (1983).

[11] Y. Cai, T. Han, T. Li, and R. Ruiz, Lepton number violation: Seesaw models and their collider tests, Front. Phys. **6**, 40 (2018).

[12] A. Ferrari, J. Collot, M.-L. Andrieux, B. Belhorma, P. de Saintignon, J.-Y. Hostachy, P. Martin, and M. Wielers, Sensitivity study for new gauge bosons and right-handed Majorana neutrinos in *pp* collisions at $s = 14$ TeV, Phys. Rev. D **62**, 013001 (2000).

[13] M. Nemevsek, F. Nesti, G. Senjanovic, and Y. Zhang, First limits on left-right symmetry scale from LHC data, Phys. Rev. D **83**, 115014 (2011).

[14] J. Gluza, T. Jelinski, and R. Szafron, Lepton number violation and "Diracness" of massive neutrinos composed of Majorana states, Phys. Rev. D **93**, 113017 (2016).

[15] M. Mitra, R. Ruiz, D. J. Scott, and M. Spannowsky, Neutrino jets from high-mass W_R gauge bosons in TeV-scale left-right symmetric models, Phys. Rev. D **94**, 095016 (2016).

[16] M. Aaboud *et al.* (ATLAS Collaboration), Search for heavy Majorana or Dirac neutrinos and right-handed W gauge bosons in final states with two charged leptons and two jets at $\sqrt{s} = 13$ TeV with the ATLAS detector, J. High Energy Phys. 01 (2019) 016.

[17] A. Tumasyan *et al.* (CMS Collaboration), Search for a right-handed W boson and a heavy neutrino in proton-proton collisions at $\sqrt{s} = 13$ TeV, J. High Energy Phys. 04 (2022) 047.

[18] G. Aad *et al.* (ATLAS Collaboration), Search for heavy Majorana or Dirac neutrinos and right-handed W gauge bosons in final states with charged leptons and jets in pp collisions at $\sqrt{s} = 13$ TeV with the ATLAS detector, arXiv:2304.09553.

[19] M. Aaboud *et al.* (ATLAS Collaboration), Search for a right-handed gauge boson decaying into a high-momentum heavy neutrino and a charged lepton in pp collisions with the ATLAS detector at $\sqrt{s} = 13$ TeV, Phys. Lett. B **798**, 134942 (2019).

[20] A. Tumasyan *et al.* (CMS Collaboration), Search for new physics in the lepton plus missing transverse momentum final state in proton-proton collisions at $\sqrt{s} = 13$ TeV, J. High Energy Phys. 07 (2022) 067.

[21] G. Aad *et al.* (ATLAS Collaboration), Search for new resonances in mass distributions of jet pairs using 139 fb^{-1} of pp collisions at $\sqrt{s} = 13$ TeV with the ATLAS detector, J. High Energy Phys. 03 (2020) 145.

[22] A. M. Sirunyan *et al.* (CMS Collaboration), Search for high mass dijet resonances with a new background prediction method in proton-proton collisions at $\sqrt{s} = 13$ TeV, J. High Energy Phys. 05 (2020) 033.

[23] ATLAS Collaboration, Search for vector boson resonances decaying to a top quark and a bottom quark in the hadronic

final state using pp collisions at $\sqrt{s} = 13$ TeV with the ATLAS detector, Report No. ATLAS-CONF-2021-043, 2021.

[24] CMS Collaboration, Search for W' bosons decaying to a top and a bottom quark in leptonic final states at $\sqrt{s} = 13$ TeV, Report No. CMS-PAS-B2G-20-012, 2023.

[25] CMS Collaboration, Search for new heavy resonances decaying to WW, WZ, ZZ, WH, or ZH boson pairs in the all-jets final state in proton-proton collisions at $\sqrt{s} = 13$ TeV, arXiv:2210.00043.

[26] M. Nemevšek, F. Nesti, and G. Popara, Keung-Senjanović process at the LHC: From lepton number violation to displaced vertices to invisible decays, Phys. Rev. D **97,** 115018 (2018).

[27] G. Beall, M. Bander, and A. Soni, Constraint on the Mass Scale of a Left-Right Symmetric Electroweak Theory from the $K_L - K_S$ Mass Difference, Phys. Rev. Lett. **48,** 848 (1982).

[28] G. Senjanović and P. Senjanović, Suppression of Higgs strangeness changing neutral currents in a class of gauge theories, Phys. Rev. D **21,** 3253 (1980).

[29] G. Ecker and W. Grimus, CP violation and left-right symmetry, Nucl. Phys. **B258,** 328 (1985).

[30] R. N. Mohapatra, G. Senjanovic, and M. D. Tran, Strangeness changing processes and the limit on the right-handed gauge boson mass, Phys. Rev. D **28,** 546 (1983).

[31] Y. Zhang, H. An, X. Ji, and R. N. Mohapatra, Right-handed quark mixings in minimal left-right symmetric model with general CP violation, Phys. Rev. D **76,** 091301 (2007).

[32] A. Maiezza, M. Nemevšek, F. Nesti, and G. Senjanović, Left-right symmetry at LHC, Phys. Rev. D **82,** 055022 (2010).

[33] S. Bertolini, J. O. Eeg, A. Maiezza, and F. Nesti, New physics in ϵ' from gluomagnetic contributions and limits on left-right symmetry, Phys. Rev. D **86,** 095013 (2012); **93,** 079903(E) (2016).

[34] S. Bertolini, A. Maiezza, and F. Nesti, Present and future K and B meson mixing constraints on TeV scale left-right symmetry, Phys. Rev. D **89,** 095028 (2014).

[35] A. Maiezza, M. Nemevšek, and F. Nesti, Perturbativity and mass scales in the minimal left-right symmetric model, Phys. Rev. D **94,** 035008 (2016).

[36] A. Maiezza, G. Senjanović, and J. C. Vasquez, Higgs sector of the minimal left-right symmetric theory, Phys. Rev. D **95,** 095004 (2017).

[37] A. Maiezza and M. Nemevšek, Strong P invariance, neutron electric dipole moment, and minimal left-right parity at LHC, Phys. Rev. D **90,** 095002 (2014).

[38] S. Bertolini, A. Maiezza, and F. Nesti, Kaon CP violation and neutron EDM in the minimal left-right symmetric model, Phys. Rev. D **101,** 035036 (2020).

[39] A. Maiezza and F. Nesti, Parity from gauge symmetry, Eur. Phys. J. C **82,** 491 (2022).

[40] S. Bertolini, L. Di Luzio, and F. Nesti, Axion-Mediated Forces, CP Violation and Left-Right Interactions, Phys. Rev. Lett. **126,** 081801 (2021).

[41] T. G. Rizzo, Exploring new gauge bosons at a 100 TeV collider, Phys. Rev. D **89,** 095022 (2014).

[42] J. N. Ng, A. de la Puente, and B. W.-P. Pan, Search for heavy right-handed neutrinos at the LHC and beyond in the same-sign same-flavor leptons final state, J. High Energy Phys. 12 (2015) 172.

[43] P. S. B. Dev, D. Kim, and R. N. Mohapatra, Disambiguating seesaw models using invariant mass variables at hadron colliders, J. High Energy Phys. 01 (2016) 118.

[44] R. N. Mohapatra, G. Yan, and Y. Zhang, Ameliorating Higgs induced flavor constraints on TeV scale W_R, Nucl. Phys. **B948,** 114764 (2019).

[45] X. Cid Vidal et al., Report from Working Group 3: Beyond the Standard Model physics at the HL-LHC and HE-LHC, CERN Yellow Rep. Monogr. **7,** 585 (2019).

[46] R. Ruiz, Lepton number violation at colliders from kinematically inaccessible gauge bosons, Eur. Phys. J. C **77,** 375 (2017).

[47] M. Nemevšek, G. Senjanović, and V. Tello, Connecting Dirac and Majorana Neutrino Mass Matrices in the Minimal Left-Right Symmetric Model, Phys. Rev. Lett. **110,** 151802 (2013).

[48] G. Senjanović and V. Tello, Probing Seesaw with Parity Restoration, Phys. Rev. Lett. **119,** 201803 (2017).

[49] G. Senjanović and V. Tello, Disentangling the seesaw mechanism in the minimal left-right symmetric model, Phys. Rev. D **100,** 115031 (2019).

[50] J. Kiers, K. Kiers, A. Szynkman, and T. Tarutina, Disentangling the seesaw mechanism in the left-right model: An algorithm for the general case, Phys. Rev. D **107,** 075001 (2023).

[51] V. Tello, M. Nemevšek, F. Nesti, G. Senjanović, and F. Vissani, Left-Right Symmetry: From LHC to Neutrinoless Double Beta Decay, Phys. Rev. Lett. **106,** 151801 (2011).

[52] J. Barry and W. Rodejohann, Lepton number and flavour violation in TeV-scale left-right symmetric theories with large left-right mixing, J. High Energy Phys. 09 (2013) 153.

[53] F. Bezrukov, H. Hettmansperger, and M. Lindner, keV sterile neutrino dark matter in gauge extensions of the Standard Model, Phys. Rev. D **81,** 085032 (2010).

[54] M. Nemevsek, G. Senjanovic, and Y. Zhang, Warm dark matter in low scale left-right theory, J. Cosmol. Astropart. Phys. 07 (2012) 006.

[55] M. Nemevšek and Y. Zhang, Dark Matter Dilution Mechanism through the Lens of Large-Scale Structure, Phys. Rev. Lett. **130,** 121002 (2023).

[56] G. Barenboim, K. Huitu, J. Maalampi, and M. Raidal, Constraints on doubly charged Higgs interactions at linear collider, Phys. Lett. B **394,** 132 (1997).

[57] K. Huitu, J. Maalampi, A. Pietila, and M. Raidal, Doubly charged Higgs at LHC, Nucl. Phys. **B487,** 27 (1997).

[58] J. Maalampi and N. Romanenko, Single production of doubly charged Higgs bosons at hadron colliders, Phys. Lett. B **532,** 202 (2002).

[59] A. Roitgrund and G. Eilam, Search for like-sign dileptons plus two jets signal in the framework of the manifest left-right symmetric model, J. High Energy Phys. 01 (2021) 031.

[60] A. Maiezza, M. Nemevšek, and F. Nesti, Lepton Number Violation in Higgs Decay at LHC, Phys. Rev. Lett. **115,** 081802 (2015).

[61] M. Nemevšek, F. Nesti, and J. C. Vasquez, Majorana Higgses at colliders, J. High Energy Phys. 04 (2017) 114.

[62] J. Alwall, P. Demin, S. de Visscher, R. Frederix, M. Herquet, F. Maltoni, T. Plehn, D. L. Rainwater, and T. Stelzer, Graph/MadEvent v4: The new web generation, J. High Energy Phys. 09 (2007) 028.

[63] T. Sjostrand, S. Mrenna, and P. Z. Skands, A brief introduction to PYTHIA 8.1, Comput. Phys. Commun. **178**, 852 (2008).

[64] J. de Favereau, C. Delaere, P. Demin, A. Giammanco, V. Lemaître, A. Mertens, and M. Selvaggi (DELPHES 3), A modular framework for fast simulation of a generic collider experiment, J. High Energy Phys. 02 (2014) 057.

[65] M. Selvaggi *et al.* (FCC-hh Collaboration), Official DELPHES card prepared by FCC-hh Collaboration, Dec, 2017, https://hep-fcc.github.io/FCCSW/.

[66] M. L. Mangano *et al.*, *Physics at the FCC-hh, a 100 TeV pp Collider* (CERN, Geneva, 2017), Vol. 3.

[67] M. Nemevšek and F. Nesti, LRSM FeynRules model file, version 1.7, 2020, https://sites.google.com/site/leftrighthep/1-lrsm-feynrules.

[68] A. Roitgrund, G. Eilam, and S. Bar-Shalom, Implementation of the left-right symmetric model in FeynRules, Comput. Phys. Commun. **203**, 18 (2016).

[69] ATLAS Collaboration, Search for a new heavy gauge boson resonance decaying into a lepton and missing transverse momentum in 36 fb^{-1} of pp collisions at $\sqrt{s} = 13$ TeV with the ATLAS experiment, Report No. ATLAS-CONF-2017-016, 2017.

[70] R. N. Mohapatra and G. Senjanović, Neutrino masses and mixings in gauge models with spontaneous parity violation, Phys. Rev. D **23**, 165 (1981).

[71] M. Doi, T. Kotani, and E. Takasugi, Double beta decay and Majorana neutrino, Prog. Theor. Phys. Suppl. **83**, 1 (1985).

[72] M. Hirsch, H. V. Klapdor-Kleingrothaus, and O. Panella, Double beta decay in left-right symmetric models, Phys. Lett. B **374**, 7 (1996).

[73] J. D. Vergados, The neutrinoless double beta decay from a modern perspective, Phys. Rep. **361**, 1 (2002).

[74] M. Nemevsek, F. Nesti, G. Senjanovic, and V. Tello, Neutrinoless double beta decay: Low left-right symmetry scale? arXiv:1112.3061.

[75] C. Di Paolo, F. Nesti, and F. L. Villante, Phase space mass bound for fermionic dark matter from dwarf spheroidal galaxies, Mon. Not. R. Astron. Soc. **475**, 5385 (2018).

[76] J. A. Dror, D. Dunsky, L. J. Hall, and K. Harigaya, Sterile neutrino dark matter in left-right theories, J. High Energy Phys. 07 (2020) 168.

[77] G. Dvali, A. Maiezza, G. Senjanovic, and V. Tello, Neutrinoless double beta decay as seen by the devil's advocate, arXiv:2303.17261.

[78] A. Avasthi *et al.*, Kiloton-scale xenon detectors for neutrinoless double beta decay and other new physics searches, Phys. Rev. D **104**, 112007 (2021).